Journal of
Applied Crystallography
ISSN 0021-8898

Received 5 May 2004
Accepted 29 November 2004

Rietveld texture analysis of complex oxides: examples of polyphased Bi2223 superconducting and Co349 thermoelectric textured ceramics characterization using neutron and X-ray diffraction

Emmanuel Guilmeau,[a,b] Daniel Chateigner,[b]* Jacques Noudem,[b] Ryoji Funahashi,[a] Shigeru Horii[c] and Bachir Ouladdiaf[d]

[a]National Institute of Advanced Industrial Science and Technology, Midorigaoka, Ikeda, Osaka 563-8577, Japan, [b]CRISMAT-ENSICAEN Laboratory, UMR CNRS 6508, 6 Bd. Maréchal Juin, 14050 Caen Cedex, France, [c]Department of Superconductivity, University of Tokyo, Tokyo 113-8656, Japan, and [d]ILL, BP 156, 38042 Grenoble, France. Correspondence e-mail: daniel.chateigner@ensicaen.fr

Orientation distributions of cobaltite thermoelectric and polyphased bismuth-based cuprate superconducting textured materials are determined from neutron and X-ray diffraction analysis. Curved position-sensitive detectors coupled to a tilt-angle (χ) scan enable the treatment of the whole diffraction pattern using the combined Rietveld–WIMV–Popa algorithm. The textures of three phases of superconducting compounds are determined. The critical current densities, measured for four samples, are strongly dependent on the calculated texture strengths, crystallite sizes and phase ratios. For the cobaltite compounds, a comparison between X-ray and neutron analysis shows the advantages of the latter technique for avoiding the limitations of the X-ray analysis with respect to the defocusing effect. The results highlight the necessity and efficiency of the combined approach for a quantitative texture analysis of complex materials and exemplify the texture–anisotropic physical properties relationship for a better understanding and design of improved bulk superconducting and thermoelectric materials.

1. Introduction

Texture analysis is increasingly recognized as an important tool in the characterization of many polycrystalline materials in order to understand how intrinsic anisotropic properties are revealed at the macroscopic level in certain sample directions, and to optimize methods or process parameters. For example, the development of texture in $Ca_3Co_4O_9$ (Co349) thermoelectric and $(Bi,Pb)_2Sr_2Ca_2Cu_3O_{10}$ (Bi2223) superconducting materials is required to increase respectively their electrical conductivity and critical current densities. Because of their high structural anisotropy (Masset *et al.*, 2000; Fujii *et al.*, 2001), the alignment of plate-like grains by mechanical and/or chemical processes is necessary to attain macroscopic properties comparable with the intrinsic crystallographic properties. However, a quantitative texture analysis of these materials is not a simple task. The modulated structure of layered cobaltites and the presence of several textured phases present in bismuth-based superconductors remain a handicap in the characterization using diffraction techniques. The diffraction spectra are also very complex with many partially or fully overlapped diffraction peaks. The small number of quantitative texture studies on Bi2223 superconductors (Wenk *et al.*, 1996; Gottschalck *et al.*, 2002; Frello *et al.*, 1999; Fahr *et al.*, 2001) and the absence of any, to our knowledge, on cobaltite compounds, highlight the different problems encountered with these materials. Usually, textures are determined by extracting pole figures from single diffraction peaks, but this is difficult if pole figures overlap. To overcome this problem, the combination of Rietveld (Rietveld, 1969), Williams–Imhof–Matthies–Vinel (WIMV) (Matthies & Vinel, 1982) and Popa approaches (Popa, 1998), for instance as implemented in the *MAUD* software (Lutterotti *et al.*, 1999), permits a comprehensive new approach to crystal structure–texture–microstructure analysis. The increasing number of papers based on such a methodology illustrates the interest of many researchers in materials science in Rietveld texture analysis (Guilmeau, Lambert *et al.*, 2003; Guilmeau, Chateigner *et al.*, 2004; Wenk *et al.*, 2001, 2003; Morales *et al.*, 2002, 2003; Bae *et al.*, 2002; Xie *et al.*, 2003; Lutterotti *et al.*, 1997; Noudem *et al.*, 2004). Through these different studies, it has become apparent that the methodology readily handles fibre textures and is also valuable for textures exhibiting no peculiar symmetry, and really effective in the case of poly-

phased materials with overlapped pole figures. In the present paper, we report the first application of this method to the polyphased $(Bi,Pb)_2Sr_2Ca_2Cu_3O_{10}$ superconductor and the $Ca_3Co_4O_9$ thermoelectric compounds with fibre texture. We use neutron and X-ray analyses of samples synthesized with different process parameters to illustrate some of the possibilities and limitations of the methodology.

2. Materials

2.1. Bi-based superconductors

The samples are mixtures of two superconducting phases, $(Bi,Pb)_2Sr_2Ca_2Cu_3O_{10}$ (Bi2223), and $(Bi,Pb)_2Sr_2CaCu_2O_8$ (Bi2212), and one alkaline earth cuprate phase, $(Sr,Ca)_{14}Cu_{24}O_{41}$ (14:24), in residual content. Four samples were prepared by the newly developed calcination-sinter-forging method (CSF) (Guilmeau *et al.*, 2002) using 20, 50, 100 and 150 h sinter-forging dwell times, respectively. Starting from calcined powders composed of Bi2212 and a secondary phases such as Ca_2PbO_4, Ca_2CuO_3 or CuO, the thermo-mechanical treatment (temperature and uniaxial pressure) allows simultaneously the nucleation and growth of the Bi2223 onto the Bi2212 and the alignment of both Bi2212 and Bi2223 plate-like grains. The resulting superconducting phases are strongly textured, with their mean *c* axes parallel to the pressure direction and consequently perpendicular to the disc surface (Fig. 1). In Fig. 2, the X-ray diffraction pattern of the disc surface illustrates the strong (00*l*) textures of both superconducting phases and the presence of the secondary '14:24' phase. The increase of the sinter-forging dwell time is employed here in order to obtain a material composed of the highest content in Bi2223 and, consequently, to improve superconducting properties. The grain alignment is also crucial in order to optimize the transport properties of the materials.

2.2. Co349 thermoelectrics

A magnetically *c*-axis aligned sample has been prepared by a slip-casting process using fine Co349 powder with an average grain size of ~3 μm in diameter. Details of the preparation are as follows. The Co349 fine powder obtained through a ball-milling process was mixed with solvent (water) and dispersant (polycarboxylic ammonium) to form a slurry. The slurry was cast into a cylindrical die under a magnetic field of 3 T applied parallel to the cylinder. Note that the die consists of a cylindrical Pyrex glass and a porous alumina plate and therefore only the solvent in the slurry is evacuated through the bottom plate. The slip-cast pellet was pressed in a cold isostatic condition at 392 MPa and then heated at 473 K for 2 h and 673 K for 3 h in order to remove the solvent and dispersant completely. The resulting specimen was then hot-forged (1153 K/20 h/16 MPa). The final dimensions of the sample were 25 × 15 × 4 mm.

3. Experiments

In order to calculate the orientation distribution (OD) of crystallites, which defines the texture of the materials, it is essential to acquire as many pole figures as possible for non-parallel (*hkl*) crystallographic planes. In this respect, it is necessary to sweep a broad 2θ angle range for various tilt χ and azimuth φ orientations. A first azimuthal scan was performed to check for possible specific texture symmetries, similarly as in previous works (Wenk *et al.*, 1996). As expected for uniaxially deformed materials without subsequent growth, we detected a C_∞ axis of symmetry aligned with the pressure axis in both materials. Fig. 3 is the {119} pole figure (ω = 15.917°, $\Delta\chi = 5°$, $\Delta\varphi = 5°$) which illustrates this symmetry in the case of our Bi2223 compounds. Consequently, due to this fibre texture stabilization, φ scans were not applied in this study. Furthermore, for such analysis, the use of a point detector is not reasonable. Indeed, to sweep a 2θ range from 10 to 60°, and for 19 angles of tilt (χ = 0–90°, step = 5°), weeks

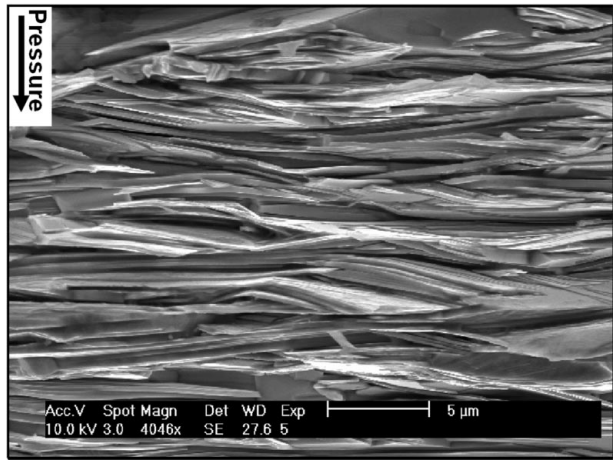

Figure 1
Typical SEM cross section of Bi2223 samples showing aligned plate-like grains. 150 h sinter-forged sample.

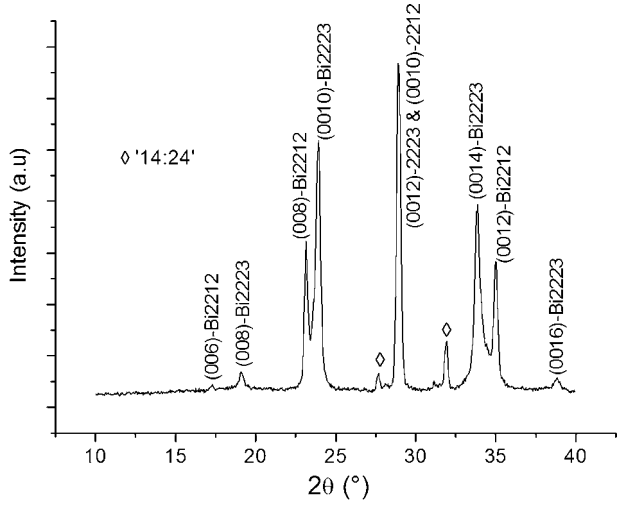

Figure 2
XRD pattern of synthesized Bi2223 discs. Main (00*l*) peaks of the Bi2212 and Bi2223 phases are indicated. Diamonds indicate the '14:24' phase. 50 h sinter-forged sample.

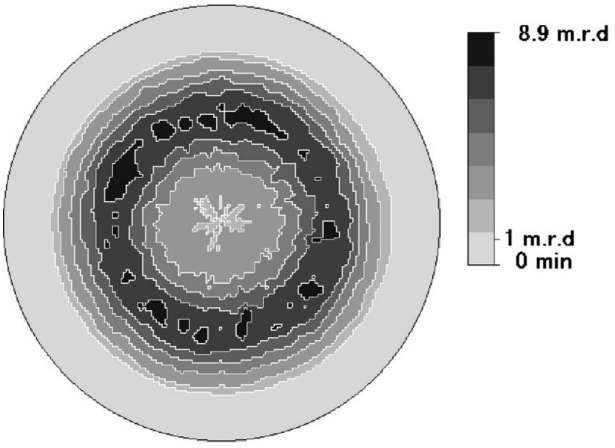

Figure 3
{119} pole figure of Bi2223 compounds with the C_∞ axis of symmetry aligned with the cylinder axis. ω = 15.917°, $\Delta\chi$ = 5°, $\Delta\varphi$ = 5°. Linear density scale, equal-area projection. 50 h sinter-forged sample. Orientation densities are calculated in multiples of random distribution (m.r.d.).

of acquisition time would be required. The well known solution to this problem is the use of a curved position-sensitive detector (Bunge *et al.*, 1982), which decreases acquisition times typically to 6 h (neutrons, ILL-D1B line) and 13 h (X-ray, CRISMAT Laboratory equipment).

Both superconducting and thermoelectric materials were analysed on the D1B neutron line at the Institut Laüe Langevin, Grenoble. The neutron wavelength is monochromated to λ = 2.523 Å. Diffracted neutrons are collected by a curved detector composed of 400 cells spread over 80° (resolution 0.2°) in 2θ. An Eulerian cradle allows χ rotations. Scans were operated over χ = 0–90° (step = 5°) using a fixed incidence angle ω of 19.84° ({0010} Bragg position) for Bi2223 superconductors, whereas an ω position of 20.6° ({003} Bragg position) was used for the cobaltites. The average volumes of our samples were around 25 and 500 mm^3 for the Bi2223 and Co349 compounds, respectively, corresponding to measuring times of around 20 min per sample orientation.

Cobalt oxides were also analysed by X-ray diffraction (XRD) with a curved position-sensitive detector (INEL CPS 120). A 1 × 1 mm collimated and parallel beam and a small vibration of the sample holder (±1 mm) were used in order to ensure that all the beam intersected the sample surface, even at high sample tilts, with a statistically relevant number of irradiated crystallites. An incidence angle of 12.5° was chosen, which corresponds to the same {003} Bragg position used with the neutron experiment. The tilt angle was scanned over χ = 0–60° (step = 5°) with an integration time of 1 h at each position. Measurements for χ values larger than 60° are too affected by beam defocusing (Chateigner *et al.*, 1992) and were not measured. The dimensions of the analysed surface were around 8 × 8 mm.

The transport critical current densities (J_c) were measured for superconducting samples by the standard four-probe technique at 77 K with an electric field criterion of 1 μV cm^{-1}. The dimensions of the samples were approximately 10 × 1.5 × 0.2 mm, with the same order of magnitude as the volume probed in the neutron experiments. Microstructures were analysed with a scanning electron microscope (SEM) (Philips XL 30 FEG).

4. Rietveld texture analysis

It would be fastidious here to describe the essence of the Rietveld texture analysis completely, which was initiated several years ago (Wenk *et al.*, 1994; Matthies *et al.*, 1997; Lutterotti *et al.*, 1997), and is described in detail elsewhere (Chateigner, 2004). However, we feel it is important to relate here, albeit briefly, the main reasons for which the Rietveld texture analysis cannot generally be avoided, *i.e.* as a non-invasive technique to probe textured samples.

Traditionally, texture analysis relies on pole-figure measurements, pole figures being measured at each required diffracted peak barycentre and rotating the sample around two θ angles (Schulz, 1949). However, this method fails for complex diffraction patterns of polyphased or low-crystal-symmetry materials, for which partial or strong peak overlap occur. In such cases, a given pole figure is composed of contributions from many (*hkl*) peaks of unknown relative contributions. In peculiar cases, these contributions can be resolved during the OD refinement procedure, but this is often not possible. This is particularly true in the case of (Bi,Pb)–Sr–Ca–Cu–O materials in which the presence of several textured phases induces analysis problems such as overlapping, preferential orientation, phase ratios, *etc*. The complex modulated structure of the Co349 phase, with many overlapping peaks, is also a serious problem. The combined approach, introducing the calculation of the OD into the Rietveld method, is in that case a very interesting tool. Briefly, after the integration of the diffracted intensities from the Le Bail algorithm (Le Bail, 1988), these intensities are used for a first refinement of the OD by WIMV analysis. The OD obtained is then introduced in the cyclic Rietveld refinement of the diagrams. The new refined parameters are used for a new WIMV cycle to correct the OD, and so on. Several cycles of refinement are performed to converge towards an 'ideal' characterization of the material. The refinement quality is assessed by a comparison of the experimental and recalculated diagrams and by the reliability factors: R_{P0} and R_{P1} for OD refinement (Lutterotti *et al.*, 1997), R_B, R_w and R_{exp} for Rietveld refinement (Young & Wiles, 1982).

Before the refinement of texture, cell parameters and crystallite size, the instrumental profile has to be calibrated. In the case of neutron analysis, a calcite sample (large crystallite sizes and no microstrains) has been used. Spectra measured in 1368 orientations were summed to reconstruct the powder pattern. This pattern is then refined to extract instrumental parameters (Caglioti, Gaussian, *etc*.). The same procedure was applied in the X-ray analysis of the SRM660 LaB_6 standard from the NIST (Balzar, 1992), which served the international round-robin calibration. The refinement was based on 13 × 4 scans measured over χ = 0–60° (step = 5°) with four φ orientations at each χ position.

After the refinement of instrumental parameters, we proceeded to refine the background as a four-degree polynomial. The final step was to refine the texture. At that time, all parameters were kept fixed (except scaling). Next, parameters related to intensity (phase ratio), broadening (crystallite size) and peak positions (cell parameters, zero offset) were refined with the texture. The Popa formalism, considering the anisotropic broadening of the diffracted peaks produced by crystallite size and microstrain, has been used. However, only the refinement of the first anisotropic size parameter led to a satisfactory spherical value independent of the anisotropic crystal shape (Fig. 1). Refining microstrains and other anisotropic crystallite size parameters did not provide a significantly better refinement (inconsistent anisotropic size parameters) nor divergence of the program.

The experience showed us that the data treatment is far from routine and requires manual intervention at every step. First, as aforementioned, the pattern presents a real complexity due to the low number of Bi2212 and Bi2223 diffraction peaks which are in most cases partially or completely overlapped. The presence of the '14:24' secondary phase contributes to the spectrum and increase the complexity of the analysis. The orthorhombic structure was used for representing the Bi2212 and Bi2223 phases. For the Co349 phase, commonly formulated as $(Ca_2CoO_3)(CoO_2)_{1.62}$, an accurate structure refinement of this misfit aperiodic phase needs a description in the superspace formalism for modulated structures. It was notably given from a four-dimensional structure refinement of three polytype phases (Lambert *et al.*, 2001). From these results, a structural model was built concerning the main phase characterized by the previously reported cell parameters. This model was then confirmed using powder neutron diffraction data (Grebille *et al.*, 2004) and the corresponding structural parameters were used to reconstruct a commensurate supercell approximant ($P2_1/m$ space group) and a resulting unit cell with a = 4.8309, b = 36.4902, c = 10.8353 Å and β = 98.1317°.

5. Results and discussion

5.1. Neutron diffraction analysis of Bi-based superconductors

Fig. 4 shows typical neutron diffraction patterns obtained from a 0–90° χ scan. This graph highlights without ambiguity the (00l) texture of both the Bi2212 and the Bi2223 phase. In particular, we can clearly observe the disappearance of the (00l) lines when χ increases to 30° and the appearance of the (220) line when χ tends to 90°. We can also note the presence of secondary peaks related to the 14:24 phase, the intensity of which decreases as χ increases. This behaviour, previously not observed to our knowledge, is significant of the texture of this phase.

Fig. 5 illustrates the refinement reliability using a selection of 19 diagrams (χ scans) typically obtained for the four samples. These spectra were measured on the sample textured at 1118 K for 150 h. In this case, only the Bi2212 and Bi2223 phases have been considered in the refinement, neglecting the '14:24' phase; the main 2θ ranges (45.8–48.2°, 52.76–55.4°) related to the stronger peaks of this phase have been removed in the analysis.

Fig. 6(*a*) shows pole figures recalculated from the OD obtained by the WIMV algorithm, based on the experimental pole figures of Fig. 6(*b*) which represent normalized intensities extracted with the Le Bail algorithm. Pole figures are related to the Bi2223 phase in the sample textured during 150 h at 1118 K. A good agreement between the experimental and recalculated pole figures is observable. It proves the efficiency of the software to treat a complex material with different phases and textures. However, the quantitative Rietveld texture analysis is not perfect. One can note a difference between the maximum of the orientation distributions of the two series of pole figures. The experimental pole figures present a maximum around 44 m.r.d. (multiples of random distribution), whereas the maximum of the recalculated ones is around 27 m.r.d. This difference, noted for all samples, is explained by the problem of overlapping between the (008) and (0010) peaks, or between the (0012) and (0014) peaks of Bi2212 and Bi2223, respectively, observable in Fig. 5 for χ positions close to 0°. The origin of this phenomenon can be explained by different reasons. First, as seen in Fig. 1, the grain shape is not equiaxial, which indicates that the peak broadening depends on the measured sample directions. Because an equiaxial size (inconsistent anisotropic crystallite sizes) was refined from the Popa model, this may be one reason why the Rietveld refinement fitting is not so good for patterns at χ positions from 0 to 20°. Another reason could be the existence of intergranular residual stresses caused by grain-to-grain interactions (Popa & Balzar, 2001). However, we could not detect any residual stresses in our samples (no peak position shift is observed when tilting the samples, at the experimental resolution) arising from whichever cause. If the two precedent hypotheses can eventually influence the Rietveld refinement fitting at low χ positions, we strongly believe that the problem of overlapping predominantly arises from intergrowths on the

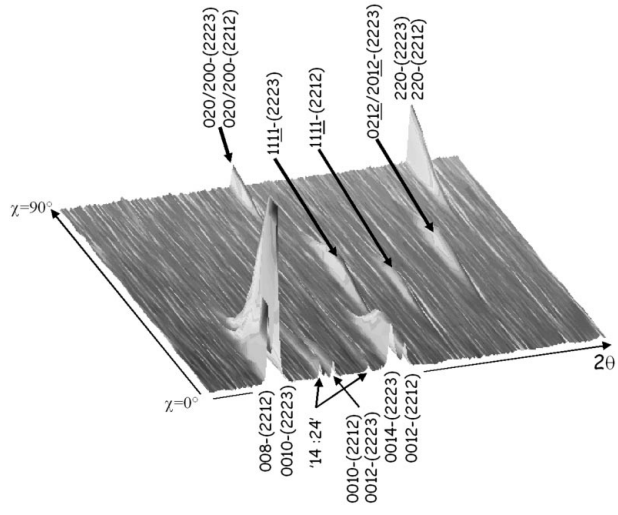

Figure 4
Neutron diffraction pattern obtained for Bi2223 samples for a 0–90° χ scan. 100 h sinter-forged sample.

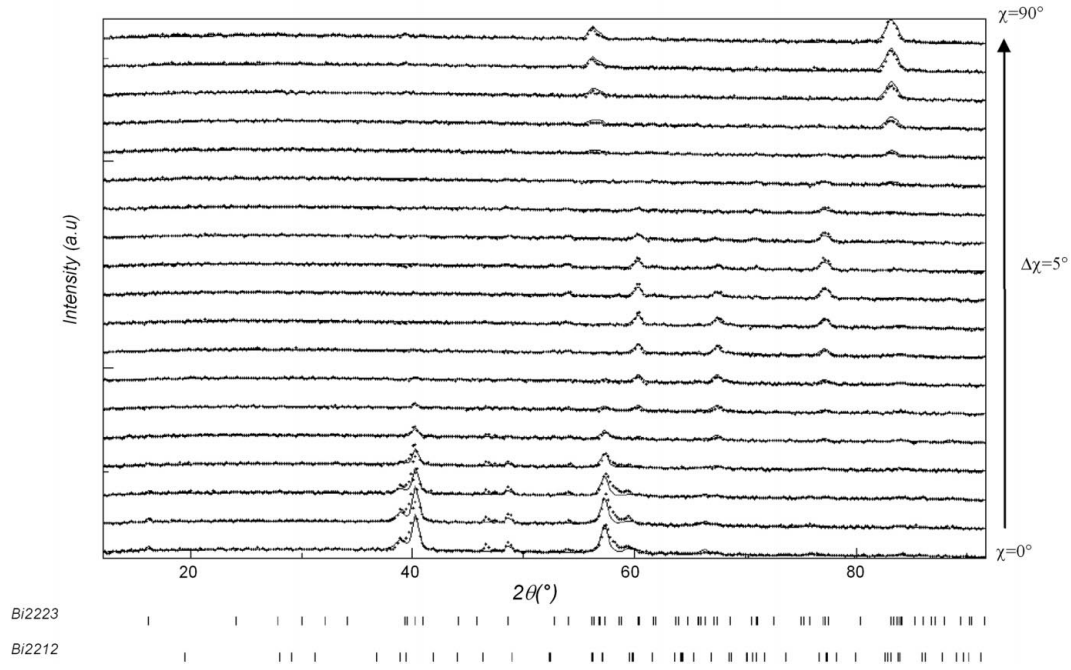

Figure 5
Experimental (dots) and calculated (lines) neutron diffraction patterns for various χ positions (0–90°). 150 h sinter-forged Bi2223 sample.

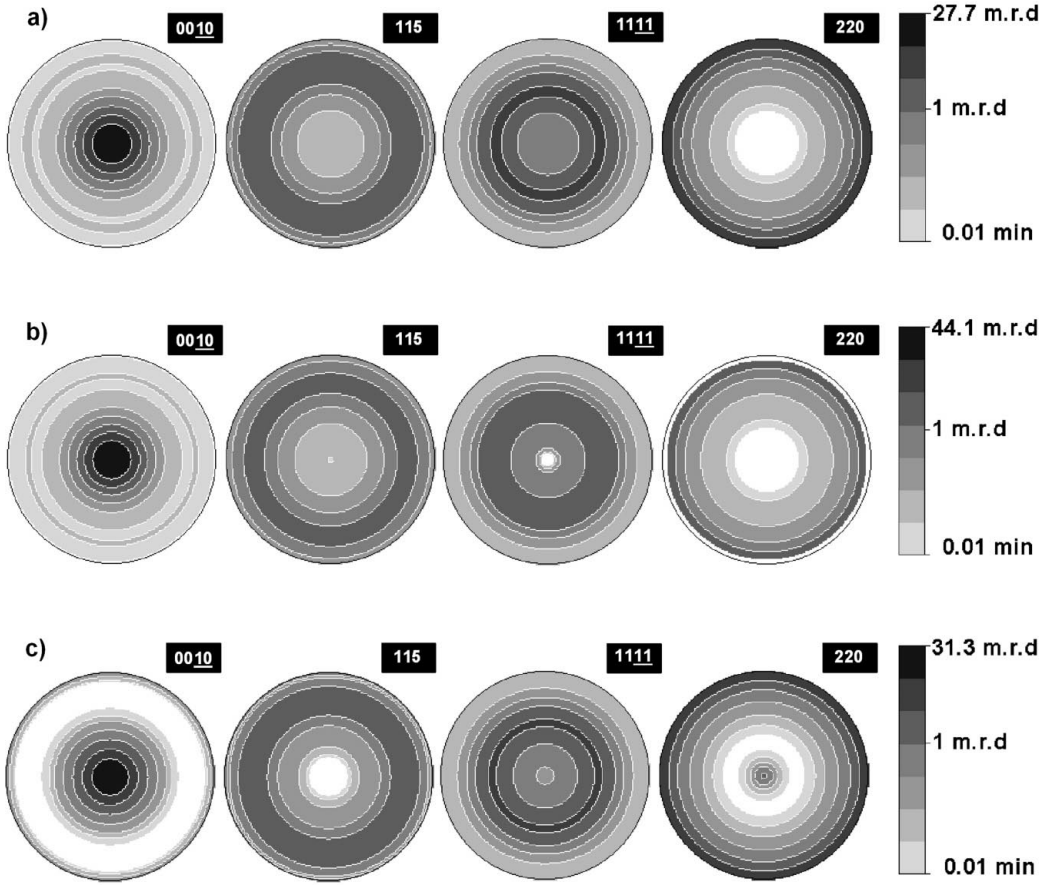

Figure 6
Selected {0010}, {115}, {1111} and {220} pole figures (*a*) recalculated from the OD obtained by the WIMV algorithm, (*b*) extracted with the Le Bail algorithm and (*c*) recalculated from incomplete pole figures (without patterns for χ positions from 0 to 20°). 150 h sinter-forged Bi2223 sample. Logarithmic density scale, equal-area projection.

Table 1
Texture index and maximum values for the ODF as obtained for the four Bi2223 samples.

Refined cell parameters, phase proportions and reliability factors are included. Transport critical current densities, measured for each sample, are also reported.

Sinter-forging dwell time (h)	Orientation distribution maximum (m.r.d.) and texture index F^2 (m.r.d.^{2})			Cell parameters (Å)		Crystallite size Bi2223 (nm)	R_B (%)	R_w (%)	R_{exp} (%)	R_{P0} (%)	R_{P1} (%)	J_c (A cm^{-2})
	Bi2212	Bi2223	% Bi2223	Bi2223	Bi2212							
20	21.8 F^2 = 9.24	20.7 F^2 = 9.86	59.9 (1.3)	a = 5.419 (3) b = 5.391 (3) c = 37.168 (3)	a = 5.414 (3) b = 5.393 (3) c = 30.800 (3)	205 (7)	7.56	11.1	4.55	17.74	10.56	12500
50	24.1 F^2 = 10.2	24.4 F^2 = 10.45	72.9 (2.9)	a = 5.419 (3) b = 5.408 (3) c = 37.192 (3)	a = 5.416 (3) b = 5.396 (3) c = 30.806 (3)	273 (10)	7.54	11.37	4.58	17.05	11.04	15000
100	31.5 F^2 = 13.9	25.2 F^2 = 10.7	84.6 (4.4)	a = 5.410 (3) b = 5.405 (3) c = 37.144 (3)	a = 5.412 (3) b = 5.403 (3) c = 30.752 (3)	303 (10)	5.4	8.04	3.69	13.54	9.31	19000
150	65.4 F^2 = 31.2	27.2 F^2 = 12.4	87.0 (4.1)	a = 5.417 (3) b = 5.403 (3) c = 37.199 (3)	a = 5.413 (3) b = 5.407 (3) c = 30.792 (3)	383 (13)	6.13	9.12	4.8	16.24	12.25	20000

c axis, namely random stacking-fault structures. This phenomenon, already observed by several authors (Ranno *et al.*, 1993; Hatano *et al.*, 1994; Ohkubo *et al.*, 1995), induces new periodicities and asymmetric peaks. New reflections appear between the two (00l) lines of the Bi2212 and Bi2223 phases and make the refinement delicate. We have not yet elucidated this problem, and no algorithm is included in the Rietveld texture analysis to address this question. This hypothesis is anyway consistent to explain the difference of maximum orientation densities. The refinement, which well reproduces the spectra at high χ positions, tends to decrease the intensity at low χ positions, resulting in the smallest texture strength of the Bi2223 phase.

Table 1 summarizes all the refined parameters [cell parameters, crystallite size, maximum of the (00l) orientation distribution (OD_{max}), phase ratio] and reliability factors obtained for each sample. Texture index (Bunge, 1982) values are included for assessing the texture strength. Transport critical current densities, measured for each sample, are also reported. The remarkable correlation between the evolution of each refined parameter and the sinter-forging dwell time indicates that, while no significant variation of the cell parameters is observed (the phases are formed in their usual state), the improvement of the critical current densities (J_c) is closely related to an increase of OD_{max}, the Bi2223 phase content and the crystallite size. The circulation of the current is not only facilitated by a better alignment of grains and a larger percentage of Bi2223, but also by a larger crystallite size, which consequently limits the number of grain boundaries and, therefore, current barriers in the material. We can also note that for 20 and 50 h dwell times, the textures of Bi2212 and Bi2223 are very closely linked, indicating the strong growing interaction between these phases. The difference occurring for longer dwell times is due to insufficient counting statistics, which are not suitable to extract exact parameters related to the Bi2212 phase. It should be noted here that a nucleation–growth mechanism between the Bi2212 and Bi2223 phases, even for long dwell time, has been established in previous works (Guilmeau, Chateigner & Noudem, 2003). In that case, X-ray analyses with a point detector and a long acquisition time are appropriate to measure *via* a quantitative analysis the textures of both the Bi2212 and Bi2223 phases. In addition, by observing the evolution of reliability factors for the different samples, we can see that the agreement between experimental and calculated spectra tends to be decreased for shorter sinter-forging times. This confirms our hypothesis on the overlapping error due to stacking faults between the Bi2212 and Bi2223 phases. The important ratio of Bi2212 phase (40.1% for 20 h and 27.1% for 50 h) implies a more pronounced effect of overlapping on the refinement (clearly visible in refined spectra) and results in larger values of the reliability factors.

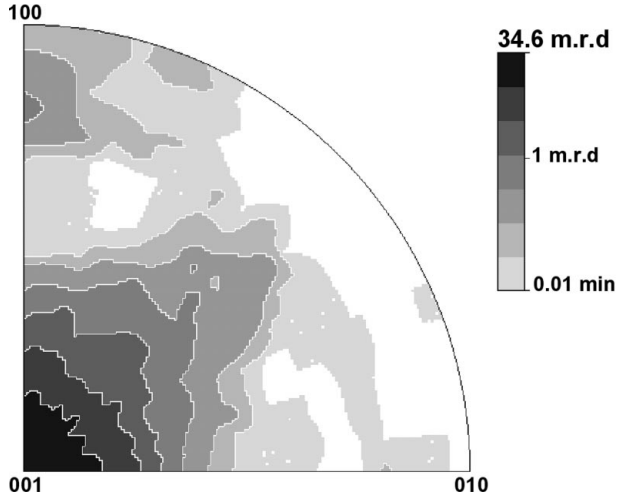

Figure 7
Inverse pole figure calculated for the fibre direction (sample's normal) for the 150 h sinter-forged Bi2223 sample. Major (001) component and small component for (10l) planes. Logarithmic density scale, equal-area projection.

Table 2
Texture index and maximum values for the ODF as obtained for the four Bi2223 samples from incomplete pole figures.

Phase proportions and reliability factors are reported.

Sinter-forging dwell time (h)	Orientation distribution maximum (m.r.d) and texture index F^2 (m.r.d.^{2}) Bi2212	Bi2223	% Bi2223	R_B (%)	R_w (%)	R_{exp} (%)	R_{P0} (%)	R_{P1} (%)
20	21.52 $F^2 = 10$	21.3 $F^2 = 10.1$	66.7 (2.6)	6.42	8.68	4.66	10.93	7.76
50	21.65 $F^2 = 10.2$	26.72 $F^2 = 10.8$	74.5 (6.4)	5.77	7.7	4.7	12.27	9.37
100	41.59 $F^2 = 15.5$	28.71 $F^2 = 11.8$	78.0 (3.0)	4.06	5.16	4.04	12.89	6.45
150	70.58 $F^2 = 30.1$	30.26 $F^2 = 14.5$	84.9 (7.6)	4.93	6.5	4.91	12.48	11.2

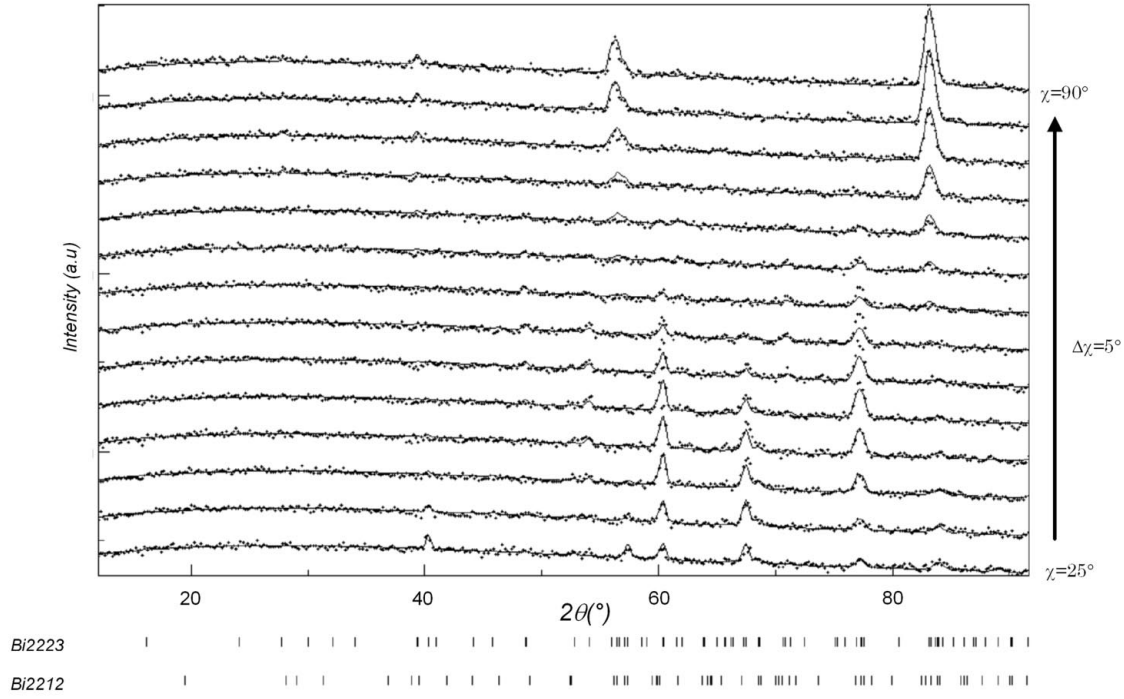

Figure 8
Experimental (dots) and calculated (lines) neutron diffraction patterns for various χ positions (25–90°). 150 h sinter-forged Bi2223 sample.

From the point of view of transport properties in the (*ab*) planes, it is important to check which (*hkl*) planes align with their normals along **z** (normal to the sample surface), which cannot be evidenced easily using pole figures alone. The full representation of the OD is needed, which in the case of fibre textures can be represented by the inverse pole figure (Fig. 7) calculated for the **z** fibre direction. In this figure, we can retrieve the previously described (001) major component with a small component for (10*l*) planes.

Because of the overlapping problem observed at low χ positions, we decided to remove the first five spectra (χ = 0–20°) for another analysis. In this way, the contribution of intergrowth is removed and we can expect to attain better reliability factors. Fig. 8 illustrates the refinement reliability for a selection of 14 diagrams (χ scans) typically obtained for the four samples. As expected, the reliability factors (presented in Table 2) are lower than those obtained with the full 19 χ-scan patterns. This decrease is explained by the avoidance of the fitting problem at low χ angles and the reduced number of diffractograms to fit. Even if few inconsistencies still exist, the whole refined neutron diffractogram is in agreement with the experimental one. We extracted the same parameters as before (except crystallite size and cell parameters, which were fixed). The results follow the same trend as before, with higher texture strengths and a narrower dispersion of the phase ratios, except for the Bi2212 phase which presents a lower texture strength for the 50 h sinter-forging dwell time. Finally, Table 2 highlights the influence of overlapping error on the quantitative Rietveld texture analysis, which results in a decrease of the texture strength

Table 3
Texture index and maximum values for the ODF as obtained for the four Bi2223 samples by using three phases (Bi2212, Bi2223 and 14:24 phases).

Phase proportions and reliability factors are included.

Sinter-forging dwell time (h)	Orientation distribution maximum (m.r.d.) with texture index F^2 (m.r.d.^{2}), Bi2223 phase	% Bi2223	% Bi2212	% 14:24	R_B (%)	R_w (%)	R_{exp} (%)	R_{P0} (%)	R_{P1} (%)
20	19.85 F^2 = 9.15	52.9 (1.0)	33 (2.3)	14.1 (0.9)	7.11	10.57	4.55	10.77	9.5
50	22.71 F^2 = 9.93	65.9 (3.3)	25.5 (1.6)	8.6 (0.7)	7.39	11.2	4.58	14.94	14.74
100	22.75 F^2 = 10.15	82.3 (5.1)	11.8 (0.9)	5.9 (1.1)	5.39	8.06	3.69	10.61	9.89
150	25.31 F^2 = 12.0	84.6 (5.7)	11.5 (1.5)	3.9 (0.6)	6.18	9.22	4.8	13.12	10.63

when the 19 χ-scan patterns are considered. Fig. 6(*c*) shows pole figures recalculated from the OD based on the experimental and incomplete pole figures (with removal of the χ = 0–20° range). Pole figures are related to the Bi2223 phase in the sample textured during 150 h at 1118 K. By comparison with pole figures recalculated from the complete poles figures (Fig. 6*a*), we can observe that smaller differences exist between the experimental and recalculated pole figures.

After these two sets of analyses with complete and incomplete pole figures, a third phase was introduced in the analysis: the '14:24' phase. The indexing of this latter phase on the neutron diffractogram (Fig. 4) is consistent with the work of Giannini *et al.* (1999), where this phase appears during the heat treatment around 1113 K. The results of the refinement are presented in Table 3. As the sinter-forging time increases, an increase of both Bi2223 content and OD_{max} can be noted, as previously. However, at the same time, we can verify that the amount of the 14:24 phase decreases. As has been explained by Giannini *et al.* (1999), the 14:24 phase content increases during the heating step and saturates when the dwell temperature is attained. Holding the temperature thus induces a decrease in the 14:24 phase. The same behaviour, observed in the frame of our study, confirms that the formation of the Bi2223 phase is correlated to the consumption of the 14:24 phase. SEM observations in electron backscattering combined with EDS analysis allowed the identification of the 14:24 secondary phases in the Bi2212 and Bi2223 textured matrix (Fig. 9). With respect to the texture refinement, the secondary phase presents a pronounced texture, as expected from the neutron diffractogram in Fig. 4. The inverse pole figure calculated for the fibre direction illustrates this texture with a maximum of the orientation distribution equal to 11.8 m.r.d. (Fig. 10), whereas the Bi2223 superconducting phase remains with the same texture. The development of the 14:24 texture, represented with a major (001) component, is still not clear however, owing to the multitude of complex structures coexisting in the material. In any case, our conclusions highlight again the strong potential of the Rietveld texture approach to analyse texture and microstructure related to several crystalline phases present in the material.

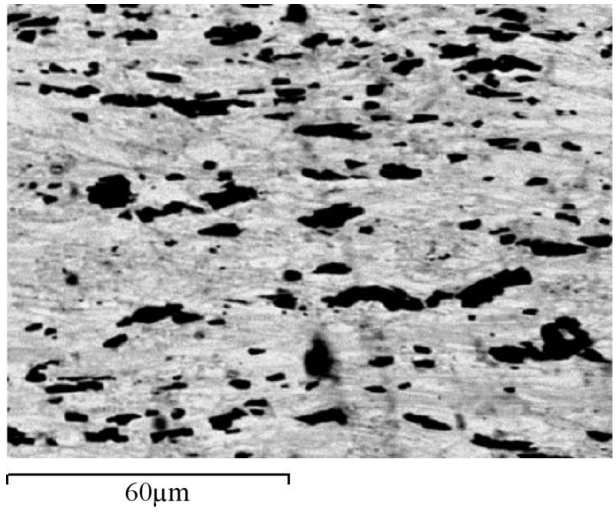

Figure 9
SEM micrograph of a polished transverse section showing the '14:24' phase (black areas). 50 h sinter-forged sample.

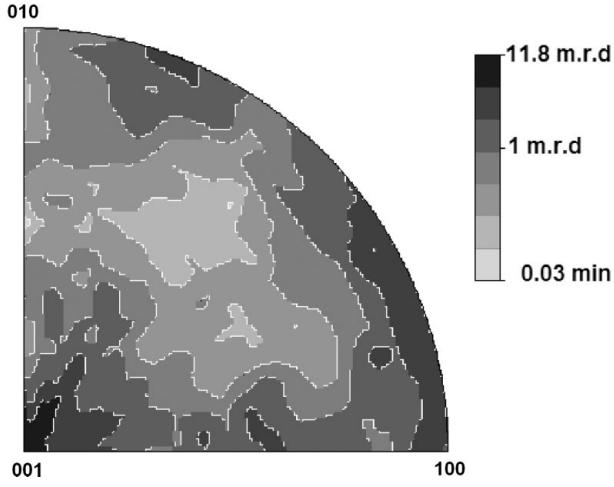

Figure 10
Inverse pole figure calculated for the fibre direction (sample's normal). '14:24' phase. Major component (11.8 m.r.d.) for (001) direction. 50 h sinter-forged sample.

5.2. X-ray/neutron analysis of Co349 thermoelectric compounds

Here we wish to illustrate the advantages of the use of neutrons with respect to an X-ray source, in the frame of cobaltite ceramics. This material has been chosen for different reasons. First, many groups are working on the elaboration of textured Co349 materials and require an accurate knowledge of the texture. We will show here the efficiency of the combined approach to extract quantitative texture informations on such complex compounds. Second, from a technical

point of view, the X-ray defocusing effect has a drastic influence on the broadening and the decrease of diffracted intensities. The resulting 2θ diagrams measured for χ positions larger than 30° do not present distinguishable diffraction peaks. This phenomenon, correlated with the incomplete pole-figure coverage, tends to complicate the refinement. The neutron investigations avoid the defocusing problem and permit equivalent diffraction of all (hkl) crystallographic planes for each χ orientation. A comparison between the two measurements is thus very interesting. Thirdly, the volume analysis ($\sim$0.5 cm^3) provided by the neutron beam is essential to confirm the high texture development of the whole sample.

The refinement proceeded in the same way as for the Bi-based superconducting compounds. After the determination of instrumental and background parameters, the texture was refined using the combined formalisms. The X-ray refinement is presented in Fig. 11, where one can appreciate the correct agreement between the experimental and refined spectra, although all high-intensity reflections appearing at inclined orientations are severely weakened due to strong defocusing, cumulating to fluorescence. The refinement reliability corresponds to R_P, R_{P1}, R_w and R_B factors equal respectively to 10.65%, 8.73%, 5.86% and 4.1%.

Fig. 12(*a*) shows the {003}, {$\bar{1}$83} and {$\bar{2}$01} pole figures recalculated from the refined OD based on the experimental pole figures which represent normalized intensities extracted with the Le Bail algorithm. In the low χ-angle range, the agreement appears to be almost correct between the two sets of pole figures. The {003} pole figures exhibits a strong centred pole, as a sign of the strong preferential orientation with *c* axes parallel to the sample normal. The {$\bar{1}$83} pole figure presents a circle with a maximum of distribution density for the χ position around 50°, which is equal to the angle between the (001) and ($\bar{1}$83) directions in the supercell structure. The maximum of distribution density around $\chi = 90°$ for the {$\bar{2}$01} pole figure is also compatible with the expected texture and structure. However, we can observe minor points illustrating incoherent reproduction of the (00*l*) fibre texture of the material. Here, as will be confirmed by neutron experiments in the next paragraph, the radial process used for the elaboration of this material was not expected to develop the following incoherences in the representation of the (00*l*) texture. For example, the {003} pole figure exhibits a distribution density greater than 1 m.r.d. for $\chi \simeq 45°$ and the calculated {$\bar{2}$01} pole figure presents a high-density circle around $\chi \simeq 65°$. These errors tend to indicate that the texture is not well reproduced and that the analysis is biased somehow. The inverse pole figure recalculated from the OD for the direction of the fibre (sample's normal) highlights also several texture components (Fig. 13*a*). The figure exhibits the intended major component with (001) planes parallel to the sample plane. According to the monoclinic structure, the 001 pole is at 98° from $\bar{1}$00. However, other broad and minor components appear, the indexing of which remains difficult due to the large number of corresponding crystallographic planes in the supercell structure. This phenomenon is, in any case, consistent with the incorrect calculated pole figures and highlights the limitations of the refinement with X-ray measurements on this cobaltite compound. Since the experiment does not cover the outer part of the pole figures, the problem is not sufficiently defined to obtain a clear solution and the absence of diffracted peaks at medium χ positions (30–60°) does not favour the refinement.

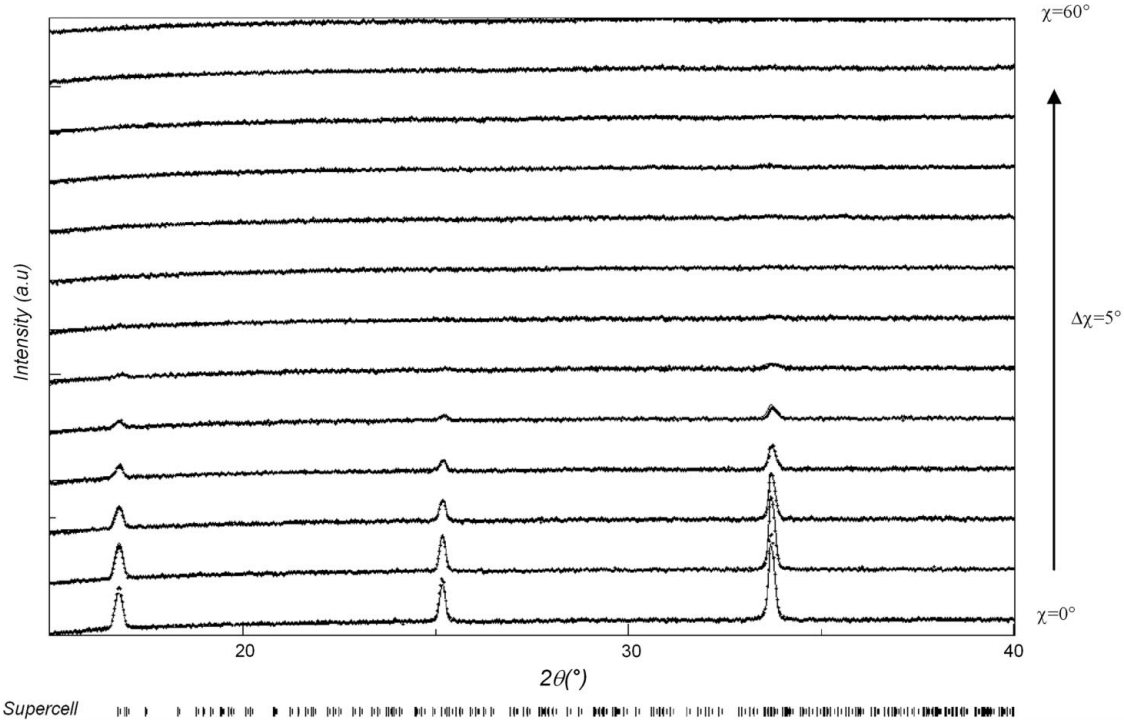

Figure 11
Experimental (dots) and refined (lines) XRD patterns for different χ positions. $Ca_3Co_4O_9$ sample.

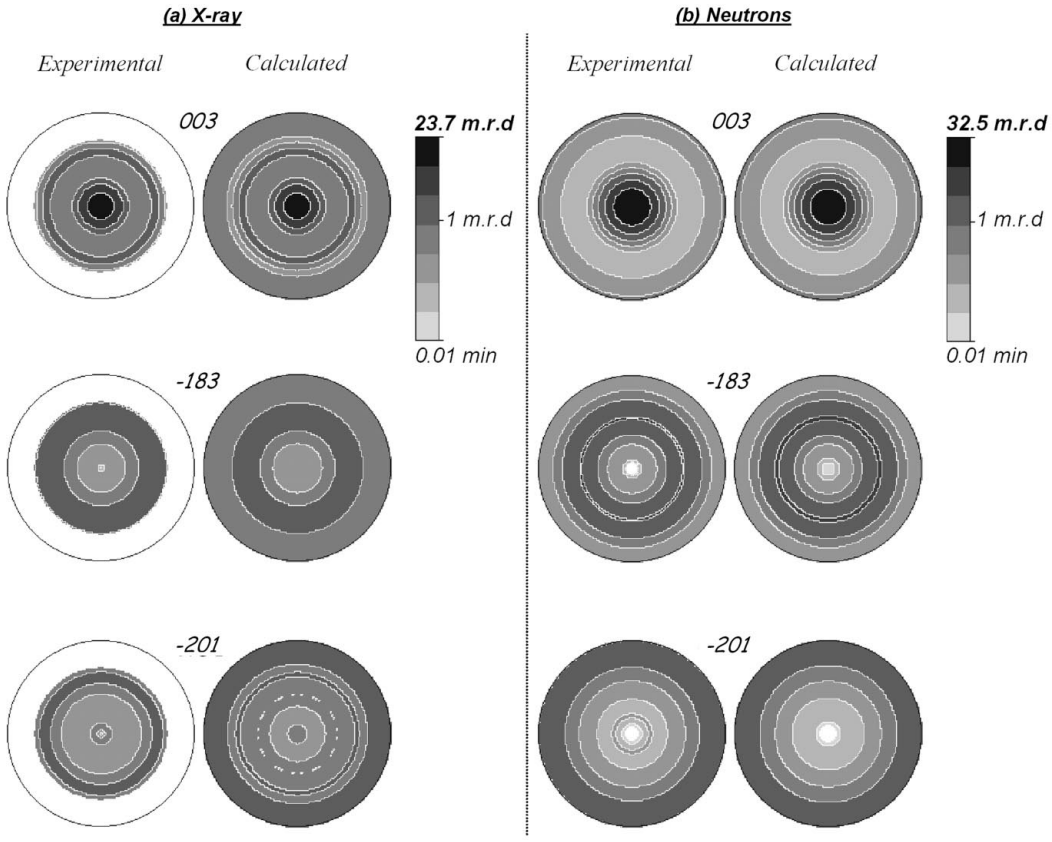

Figure 12
(*a*) X-ray and (*b*) neutron analyses of the $Ca_3Co_4O_9$ sample. Selected {003}, {$\bar{1}$83} and {$\bar{2}$01} pole figures extracted with the Le Bail algorithm (experimental) and calculated from the OD. Logarithmic density scale, equal-area projection.

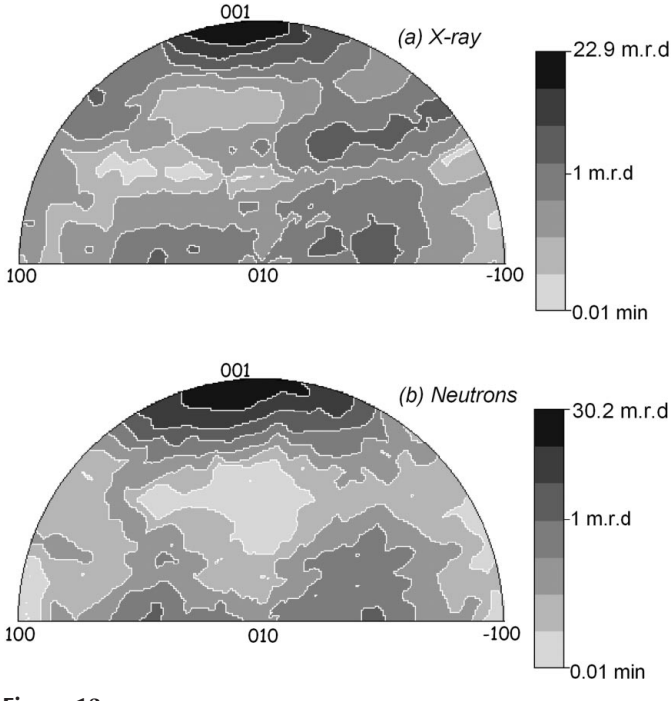

Figure 13
Inverse pole figure calculated for the fibre direction (sample's normal). (*a*) X-ray and (*b*) neutron analyses of the $Ca_3Co_4O_9$ sample. Logarithmic density scale, equal-area projection.

The additional poles could, however, come from the activation of cleavage plane systems different from the regular {00*l*} system during the applied process, and may not be artefacts resulting from insufficient pole-figure coverage.

To confirm our conviction about the limitations of the X-ray analysis and find an accurate solution, neutron diffraction was performed on the same specimen. In that case, more peaks with a non-zero intensity are available as a result of the different atomic scattering by neutrons, the defocusing effect is removed, and no fluorescence occurs, which allows all the peaks to be revealed up to $\chi = 90^\circ$ (Fig. 14). The reliability seems comparable with that of the X-ray analysis for low χ orientations, whereas the peaks indexed at $2\theta \simeq 67^\circ$ and 73° are not correctly represented by the calculated profile. Compared with the X-ray analysis, the reliability factors are larger: 19.7, 12.4, 11.9 and 8.3% for R_P, R_{P1}, R_w and R_B, respectively. This increase is attributed to the incorrect peak refinement and, of course, to the additional seven 2θ scans over $\chi = 65$–90° introduced in the refinement. The incorrect fitting at high χ positions is still not elucidated. The {003}, {$\bar{1}$83} and {$\bar{2}$01} calculated and experimental pole figures are shown in Fig. 12(*b*). No significant differences are observed between the two sets of pole figures, which proves that the neutron data reproduce the experimental texture with better accuracy. Moreover, the calculated pole figures are in agreement with

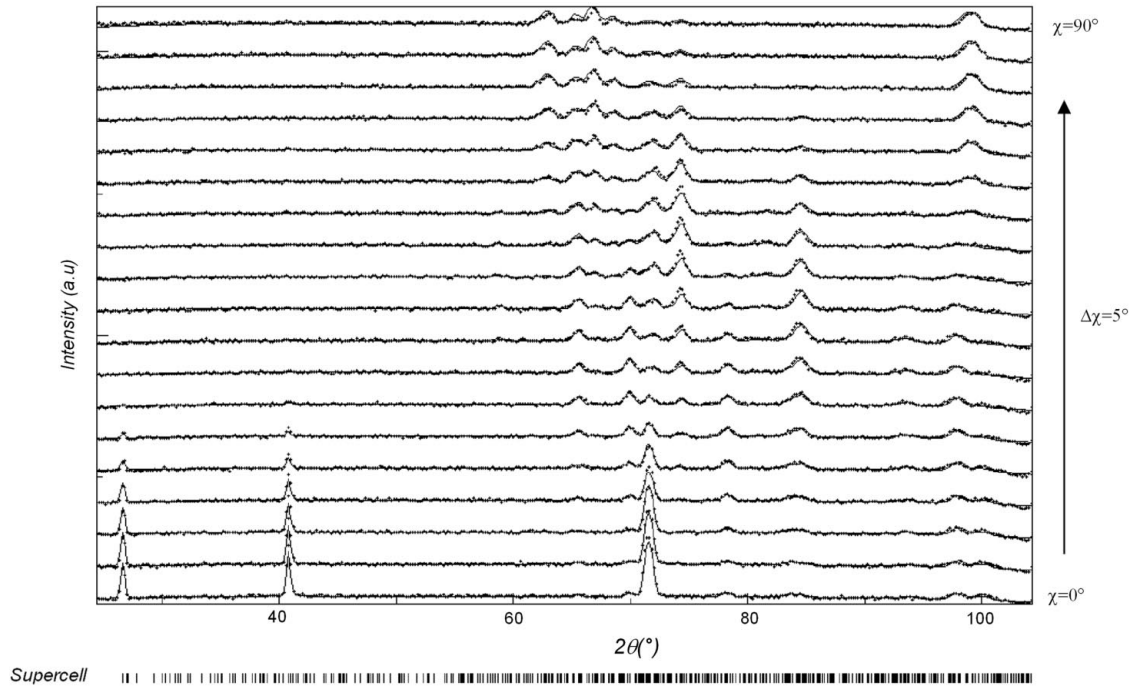

Figure 14
Neutron analysis of the $Ca_3Co_4O_9$ sample. Experimental (dots) and refined (lines) neutron diffraction patterns for different χ positions.

the theoretical (00*l*) texture. No parasitic orientation densities are observed on the three pole figures, except for the {003} with a circle (density < 1 m.r.d.) at $\chi \simeq 90°$. The inverse pole figure recalculated from the OD for the direction of the fibre (Fig. 13*b*) illustrates without any ambiguity the important contribution of neutron data to converge towards an accurate solution. Only one major (001) pole is observed with a maximum of density higher than those calculated from X-ray data. One minor pole with a density close to 1 m.r.d. can be noted, corresponding to a fairly low volume fraction of material compared with the main component. These results confirm our hypothesis on the limitations of the X-ray analysis in the frame of our study on $Co_3Ca_4O_9$ reactive-templated grain-growth (RTGG) compounds (Guilmeau, Itahara *et al.*, 2004). Indeed, we also reported the presence of parasitic poles on the inverse pole figures, which advised us to be cautious in explaining the mechanisms leading to such inconsistencies. The neutron measurements detailed in the present paper provide the answer to our doubts.

6. Conclusion

This study, based on neutron and X-ray analysis using curved position-sensitive detectors, has demonstrated the efficient and reliable use of an iterative combination of algorithms implemented in the Rietveld methodology for OD calculation (WIMV) and crystallite size determination (Popa). The *MAUD* package, which implements these algorithms, offers possibilities for quantitative texture analysis of polyphased materials. This approach permits the correlation of physical properties with texture strength, microstructure aspects, *etc.*, and particularly highlights the importance of texture analysis for a better understanding and design of real non-destructible superconducting and thermoelectric materials for practical applications.

DC gratefully acknowledges the French Ministère de la Recherche et de la Technologie and the Délégation Régionale à la Recherche et à la Technologie – région Basse-Normandie, for financial support of the X-ray experimentation.

References

Bae, J.-H., Heo, G., Oh, S. T., Shin, E., Seong, B.-S., Lee, C.-H. & Oh, K. H. (2002). *Mater. Sci. Forum*, **408–412**, 215–220.
Balzar, D. (1992) *J. Appl. Cryst.* **25**, 559–570.
Bunge, H.-J. (1982) *Texture Analysis in Materials Science*. London: Butterworths.
Bunge, H.-J., Wenk H.-R. & Pannetier J. (1982). *Texture Microstruct.* **5**, 153–170.
Chateigner, D. (2004). http://www.ensicaen.ismra.fr/~chateign/texture/combined.pdf.
Chateigner, D., Pernet, M. & Germi, P. (1992). *J. Appl. Cryst.* **25**, 766–769.
Fahr, T., Trinks, H.-P., Schneider, R. & Fischer, C. (2001). *IEEE Trans. Appl. Supercond.* **11**, 3399–3402
Frello, T., Poulsen, H. F., Gottschalck Andersen, L., Andersen, N. H., Bentzon, M. D. & Schmidberger, J. (1999). *Supercond. Sci. Technol.* **12**, 293–300.
Fujii, T., Watanabe, T. & Matsuda, A. (2001). *J. Cryst. Growth*, **223**, 175–180.
Giannini, E., Bellingeri, E., Passerini, R. & Flükiger, R. (1999). *Physica C*, **315**, 185–197.

Gottschalck Andersen, L., Poulsen, H. F., Abrahamsen, A. B., Jacobsen, B. A. & Tschentscher, T. (2002). *Supercond. Sci. Technol.* **15**, 190–201.
Grebille, D., Lambert, S., Bourée, F. & Petricek, V. (2004). *J. Appl. Cryst.* Submitted.
Guilmeau, E., Chateigner, D. & Noudem, J. G. (2002). *Supercond. Sci. Technol.* **15**, 1436–1444.
Guilmeau, E., Chateigner, D. & Noudem, J. G. (2003). *Supercond. Sci. Technol.* **16**, 484–491.
Guilmeau, E., Chateigner, D., Suzuki, T. S., Sakka, Y., Henrist, C. & Ouladdiaf, B. (2004). *Chem. Mater.* In the press.
Guilmeau, E., Itahara, H., Tani, T., Chateigner, D. & Grebille, D. (2004). *J. Appl. Phys.* In the press.
Guilmeau, E., Lambert, S., Chateigner, D., Noudem, J. G. & Ouladdiaf, B. (2003). *Mater. Sci. Eng. B*, **104**, 107–112.
Hatano, T., Nakamura, K., Narita, H., Sato, J., Ikeda, S. & Ishii, A. (1994). *J. Appl. Phys.* **75**, 2141–2148.
Lambert, S., Leligny, H. & Grebille, D. (2001). *J. Solid. State. Chem.* **160**, 322–331.
Le Bail, A. (1988). *Mater. Res. Bull.* **23**, 447–452.
Lutterotti, L., Matthies, S. & Wenk, H.-R. (1999). *Proceedings of the 20th International Conference on Textures of Materials*, Vol. 2, edited by J. A. Szpunar, pp. 1599–1604. Montreal: NRC Research Press.
Lutterotti, L., Matthies, S., Wenk, H.-R., Schultz, A. S. & Richardson, J. (1997). *J. Appl. Phys.* **81**, 594–600.
Masset, A. C., Michel, C., Maignan, A., Hervieu, M., Toulemonde, O., Studer, F., Raveau, B. & Hejtmanek, J. (2000). *Phys. Rev. B*, **62**, 166–175.
Matthies, S., Lutterotti, L. & Wenk, H.-R. (1997). *J. Appl. Cryst.* **30**, 31–42.
Matthies, S. & Vinel G. W. (1982). *Phys. Status Solidi B*, **112**, 111–120.
Morales, M., Chateigner, D. & Fruchart, D. (2003). *J. Magn. Magn. Mater.* **257**, 258–269.
Morales, M., Chateigner, D., Lutterotti, L. & Ricote, J. (2002). *Mater. Sci. Forum*, **408–412**, 113–118.
Noudem, J. G., Meslin, S., Harnois, C., Chateigner, D. & Chaud, X. (2004). *Supercond. Sci. Technol.* **17**, 931–936.
Ohkubo, M., Geerk, J., Linker, G. & Meyer, O. (1995). *Appl. Phys. Lett.* **67**, 2403–2405.
Popa, N. C. (1998). *J. Appl. Cryst.* **31**, 176–180.
Popa, N. C. & Balzar, D. (2001). *J. Appl. Cryst.* **34**, 187–195.
Ranno, L., Martinez-Garcia, D. & Perriere, J. (1993). *Phys. Rev. B*, **48**, 13945–13948.
Rietveld, H. M. (1969). *J. Appl. Cryst.* **2**, 65–71.
Schulz, L. G. (1949). *J. Appl. Phys.* **20**, 1030–1033, 1033–1036.
Wenk, H.-R., Chateigner, D., Pernet, M., Bingert, J., Hellstrom, E. & Ouladdiaf, B. (1996). *Physica C*, **272**, 1–12.
Wenk, H.-R., Cont, L., Xie, Y., Lutterotti, L., Ratschbacher, L. & Richardson, J. (2001). *J. Appl. Cryst.* **34**, 442–453.
Wenk, H.-R., Lutterotti, L. & Vogel, S. (2003). *Nucl. Instrum. Methods Phys. Res. A*, **515**, 575–588.
Wenk H.-R., Matthies, S. & Lutterotti, L. (1994). *Mater. Sci. Forum*, **157–162**, 473–480.
Xie, Y., Wenk, H.-R. & Matthies, S. (2003). *Tectonophysics*, **370**, 269–286.
Young, R. A. & Wiles, D. B. (1982). *J. Appl. Cryst.* **15**, 430–438.